The mechanics of High Pressure Compressive Shearing with application to ARMCO® steel

Laszlo Toth, Viet Vu, Satyaveer Singh Dhinwal, Yajun Zhao, Roxane Massion, Cai Chen, Casey Davis, Terry Lowe

The Mechanics of High Pressure Compressive Shearing with Application to ARMCO® Steel

Laszlo S. Toth[1,2], Viet Q. Vu[1,2], Satyaveer Singh Dhinwal[1,2], Yajun Zhao[1,2], Roxane Massion[1,2], Cai Chen[3], Casey F. Davis[4], Terry C. Lowe[4]

[1]Laboratoire d'Etude des Microstructures et de Mécanique des Matériaux (LEM3), Université de Lorraine, CNRS, Arts et Métiers ParisTech, F-57045 Metz, France

[2]Laboratory of Excellence on Design of Alloy Metals for low-mAss Structures (DAMAS), Université de Lorraine, F-57045 Metz, France

[3]Nanjing University of Science and Technology, Nanjing 210094, China

[4]George S. Ansell Dept. of Metallurgical and Materials Engineering, Colorado School of Mines, Golden CO 80401 USA

Abstract

In High Pressure Shearing (HPS) a flat sample is subjected to large shear strain by displacing one of its flat surfaces with respect to the other under high compressive force. The process is driven by non-sliding friction provided by the large compressive stress. The HPS process was first proposed by Fujioka and Horita [Materials transactions, 50 (2009) 930-933], and was applied to aluminum strips; upscaling was also developed. In the present work we introduce a modified version of HPS where the compression strain is relevant, so the new process is called High Pressure Compressive Shearing (HPCS). In HPCS, the experiments are conducted similarly to HPS but with the addition of a confining-pressure and more compression strain to increase the shear strain. This paper presents the mechanical analysis of stress and strain states during HPCS and demonstrates *in situ* measurements of stress-strain relations in ARMCO® steel subject to HPCS at room temperature up to an equivalent strain of 33.3. The strain hardening characteristics, the texture and the microstructure were analyzed. It has been shown that compression during HPCS results in a non-hydrostatic stress state and that ultimate steady state of grain fragmentation can be readily reached by HPCS.

Keywords: High Pressure Compressive Shearing; Shear testing; Severe Plastic Deformation; Plasticity; ARMCO® Steel; Ultra Fine Grain Structure

Corresponding Author: Laszlo S. Toth, Laszlo.toth@univ-lorraine.fr, Tel: +33604528208

Declarations of interest: none

1. Introduction

The application of very large strains to metals can enhance their mechanical properties, especially increasing their yield stress. A large number of Severe Plastic Deformation (SPD) processes have been developed for this purpose over the past four decades [1]. The main characteristics of SPD processes are the achievement of extremely high plastic strain with the assistance of high hydrostatic pressure and little or no change in the sample dimensions. After SPD, the deformed metal can display ultrafine-grained microstructures, in the submicron or even nanostructured range (for alloyed metals). Nevertheless, the amount of strain needed to reach the smallest possible grain size is quite large, and can be estimated to be between equivalent strains of 10 and 50.

The most widely studied SPD processes are ECAP (Equal Channel Angular Pressing [2]), HPT (High Pressure Torsion [3]) and ARB (Accumulated Roll Bonding [4]). ECAP is suitable for large size specimens but many passes are needed to reach the steady state grain size regime. HPT can readily reach the steady state in a single step, however, the samples are very small thin disks. Unfortunately, when the thickness of the disk is increased, strain localization can readily happen in its middle section [5]. Finally, ARB is a test which can be readily industrialized, nevertheless, the process is quite elaborate and requires at least 7 ARB cycles to approach the steady state. A variant of the HPT testing was proposed in 2009, called HPTT (High Pressure Tube Twisting [6]), which is an SPD technique suitable for deforming short tubes. HPTT permits deforming relatively large samples, larger than in HPT. Its only disadvantage is that the length of the tube is limited; the tube length should not normally exceed the diametric dimension of the tube. Interestingly, both HPT and HPTT produce samples in which there is a significant gradient in strain: in HPT the strain is proportional to the distance from the central rotational axis, while in HPTT the strain is about four times larger at the *internal* surface of the tube compared to the external diameter. The HPTT strain gradient was successfully modeled in [7].

Still another variant of HPT was proposed by Fujioka and Horita [8] which consists in simply shearing a strip parallel to its flat surface. They named the process High Pressure Sliding (HPS). Numerous studies have been carried out to explore the capacity of this process [9-15] and HPS was scaled up to deform samples with dimensions of 100 mm long and 10 mm wide [16].

Inspired by the HPS technique, this paper proposes a variant of the HPS process, called HPCS (High Pressure Compressive Shearing), illustrated in Fig. 1. In the present realization, we employed an existing three-axes ECAP machine to impart linear shear. Two samples (with the same dimensions) are positioned in the horizontal channel on the two opposite surfaces of a plunger. In the vertical channel a punch (Punch 3) applies a large compressive force on the ensemble. The two horizontal punches displace the plunger horizontally; Punch 1 is the driving punch applying force F_D while Punch 2 exerts a confining force F_{BP}. The two samples are sheared by the friction forces F_t. To enhance the friction and avoid slipping (or 'sliding'), both the sample surfaces and the other surfaces in contact with the samples are sand-blasted before testing. The purpose of applying a confining force is to increase the hydrostatic stress on the contact surfaces between the samples and the die, to avoid sliding. The back-pressure also helps stabilize the process (*e.g.* avoiding fracture of the plunger). Fig. 1a shows the sample shapes that one would ideally expect if only simple shear takes place, with no compression. So the shapes in the schematic in Figure 1a are oblique-angled parallelograms after shearing. However, during deformation the large compression force progressively mashes the samples, so they become thinner and elongate along the shear direction. So finally the samples take the form as shown in Fig. 1b. Apart from some differences at the left ends of the samples, the shapes of the two samples are the same after testing. There appear some small variations in their thickness, which is due to some small misalignments of the plunger.

An important element of this HPCS setup is the possibility to determine the stress and strain *in situ* by measuring the displacements and the forces directly during the processing. In this work, the mechanics of HPCS are analyzed and the equations necessary to convert the forces into stress and the displacements into strain are presented. It is generally difficult or even impossible to measure the material strength during SPD processing because the sample is fully constrained. HPTT is a process where it is readily possible [7]. In HPT, Chinh et al. [17] and Wetscher et al. [18] presented empirical approaches to derive the flow stress variations during HPT. Another difficulty is the proper calculation of the magnitude of the hydrostatic stress produced by the normal pressure. It was shown for HPTT that the axial pressure produces a fully hydrostatic stress state [7]. For HPT, it can only be valid if the test is done under full constraints conditions. In the present work, an analytic formula is obtained for the hydrostatic stress state for HPCS.

2. The mechanics of HPCS

In order to set up the stress and strain equations, first we need to examine the experimental shape changes during HPCS. Fig. 2 shows schematically how the sample changes its form during shearing. We start with a rectangular shape with initial dimensions of t_0, l_0 and w_0, for the thickness, length and width, respectively. The dimension w_0 does not change during shearing because the sample is fully constrained in the width direction between the walls of the channel. However, the thickness of the sample decreases during shearing due to a combined effect of the shear and the large normal pressure. Indeed, the deformed sample has a nearly rectangular shape, as seen in the example in Fig. 1b. In the following first we analyze the strain, and then the stress state due to HPCS. The reference system is defined in Fig. 2.

Strain state:

During deformation, the sample dimensions t_0 and l_0 change into t and l due to the applied displacement s. At any time, the length of the sample is:

$$l = l_o + s \ . \tag{1}$$

The thickness of the sample is also known from the volume constancy condition; we obtain:

$$t = t_0 \frac{l_0}{l} \ . \tag{2}$$

The strain state is plane strain with the following strain rate tensor:

$$\underline{\underline{\dot{\varepsilon}}} = \begin{pmatrix} -\dot{\varepsilon} & \dot{\gamma}/2 & 0 \\ \dot{\gamma}/2 & \dot{\varepsilon} & 0 \\ 0 & 0 & 0 \end{pmatrix} , \tag{3}$$

where $\dot{\varepsilon}$ is the thickness strain rate (it is negative), and $\dot{\gamma}$ is the shear strain rate. The accumulated normal strain is:

$$\varepsilon = \int_0^{\varepsilon} d\varepsilon = \int_{t_0}^{t} \frac{dt}{t} = \ln \frac{t}{t_0} = \ln \frac{l_0}{l_0 + s} \ . \tag{4}$$

The increment of shear strain is defined as:

$$d\gamma = \frac{ds}{t} \ . \tag{5}$$

Using Eqs. (1-2), we get:

$$d\gamma = \frac{(l_0 + s).ds}{t_0.l_0} \quad . \tag{6}$$

The accumulated shear strain is:

$$\gamma = \int_0^{\gamma} d\gamma = \frac{1}{2.t_0.l_0}\left[(l_0 + s)^2 - {l_0}^2\right]. \tag{7}$$

For the strain rates, we get them from Eqs. (4) and (7):

$$\dot{\varepsilon} = -\frac{\dot{s}}{l_0 + s} \quad , \quad \dot{\gamma} = \frac{1}{t_0.l_0}.(l_0 + s).\dot{s} \quad . \tag{8a,b}$$

The equivalent strain rate is defined according to von Mises:

$$\bar{\dot{\varepsilon}}_{eq} = \sqrt{\frac{2}{3}\dot{\varepsilon}_{ij}.\dot{\varepsilon}_{ij}} \quad . \tag{9}$$

Using Eqs. (8a,b) as well as (4) and (6) in Eq. (9) we obtain:

$$\bar{\dot{\varepsilon}}_{eq} = \dot{s}\sqrt{\frac{4}{3.(l_0 + s)^2} + \frac{(l_0 + s)^2}{3{t_0}^2.{l_0}^2}} \, . \tag{10}$$

After integration, we get the following formula for the equivalent strain:

$$\bar{\varepsilon}_{eq} = \frac{1}{\sqrt{3}a}(b - c) + \frac{1}{2\sqrt{3}}\left(\ln\left|\frac{a-b}{a+b}\right| - \ln\left|\frac{a-c}{a+c}\right|\right), \tag{11}$$

where

$$a = 2t_0 l_0 \, , \; b = \sqrt{a^2 + \left(s + l_0\right)^4} \, , \quad c = \sqrt{a^2 + l_0^4} \, .$$

<u>*Stress state:*</u>

For the present experimental setup (Fig. 1), the stress tensor is defined as:

$$\underline{\underline{\sigma}} = \begin{pmatrix} \sigma_{11} & \tau & 0 \\ \tau & \sigma_{22} & 0 \\ 0 & 0 & \sigma_{33} \end{pmatrix} \quad . \tag{12}$$

The σ_{22} component is obtained directly from the experimental data. It is defined by:

$$\sigma_{22} = F_y / \left(w.l\right) = F_y / [w.(l_0 + s)] \, . \tag{13}$$

The shear stress is calculated from the difference in horizontal forces applied by the pressing and confining punches: giving the net tangential force F_x acting on the individual samples:

$$\tau = \frac{F_x}{w_0.(l_0+s)} = \frac{F_D - F_{BP}}{2.w_0.(l_0+s)}. \tag{14}$$

There are still two other components of the stress tensor that need to be determined: σ_{11} and σ_{33}. They can be obtained with the help of an assumed yield function and the associated flow rule. For the yield function ($f(\underline{\underline{\sigma}})$), the von Mises isotropic criterion is employed here; it reads for the present stress tensor:

$$f(\underline{\underline{\sigma}}) = \frac{1}{2}\left[(\sigma_{11}-\sigma_{22})^2 + (\sigma_{22}-\sigma_{33})^2 + (\sigma_{33}-\sigma_{11})^2\right] + 3\tau^2 = \sigma_{eq}^2 \quad . \tag{15}$$

The application of the flow rule provides the following relations:

$$\dot{\varepsilon}_{11} = \dot{\lambda}\frac{\partial f}{\partial \sigma_{11}} = \dot{\lambda}(\sigma_{11}-\sigma_{22}) - \dot{\lambda}(\sigma_{33}-\sigma_{11}) = -\dot{\varepsilon} \tag{16}$$

$$\dot{\varepsilon}_{22} = \dot{\lambda}\frac{\partial f}{\partial \sigma_{22}} = -\dot{\lambda}(\sigma_{11}-\sigma_{22}) + \dot{\lambda}(\sigma_{22}-\sigma_{33}) = \dot{\varepsilon} \tag{17}$$

$$\dot{\varepsilon}_{33} = \dot{\lambda}\frac{\partial f}{\partial \sigma_{33}} = -\dot{\lambda}(\sigma_{22}-\sigma_{33}) + \dot{\lambda}(\sigma_{33}-\sigma_{11}) = 0 \tag{18}$$

$$\dot{\varepsilon}_{12} = \dot{\varepsilon}_{21} = \dot{\lambda}\frac{\partial f}{\partial \tau} = \dot{\lambda}.6\tau = \frac{\dot{\gamma}}{2} \tag{19}$$

From Eq. (18), we obtain:

$$\sigma_{33} = \frac{\sigma_{11}+\sigma_{22}}{2}. \tag{20}$$

Eqs. (16) and (17) provide:

$$\sigma_{11} = \sigma_{22} - \frac{2\dot{\varepsilon}}{3\dot{\lambda}} \quad . \tag{21}$$

Eq. (19) defines the value of $\dot{\lambda}$:

$$\dot{\lambda} = \frac{\dot{\gamma}}{12\tau}. \tag{22}$$

In this way, we obtain the following formulas for the two initially unknown normal stress components:

$$\sigma_{11} = \sigma_{22} - \frac{8\tau.\dot{\varepsilon}}{\dot{\gamma}} \quad , \qquad \sigma_{33} = \sigma_{22} - \frac{4\tau.\dot{\varepsilon}}{\dot{\gamma}} \; . \tag{23a,b}$$

Substitution of the stress components into the flow function (Eq. 15) provides the von-Mises equivalent stress:

$$\sigma_{eq} = \tau.\sqrt{3 + 48\left(\frac{\dot{\varepsilon}}{\dot{\gamma}}\right)^2} \quad . \tag{24}$$

Using this formula and the equivalent strain from Eq. (11), a stress-strain curve can be constructed.

The hydrostatic stress:

Knowing all normal components of the stress tensor, it is possible to obtain the hydrostatic stress:

$$\sigma_h = \frac{\sigma_{11} + \sigma_{22} + \sigma_{33}}{3} = \sigma_{22} - 4\tau\frac{\dot{\varepsilon}}{\dot{\gamma}}. \tag{24}$$

This formula shows that the applied compressive stress is not entirely converted into a hydrostatic stress state. The difference is in the second member on the right side of Eq. (24), in which both $\dot{\varepsilon}$ and σ_{22} are negative. Therefore, the applied normal stress contributes to the plastic deformation of the samples. The application of HPCS on ARMCO® steel that we present in the following sections will show to what extent the normal pressure contributed to the plasticity of the samples.

Multiple passes:

Eq. (11) gives the strain value that can be reached in one pass. The strain depends largely on the shear displacement. It is, however, not desirable to apply too large shear displacement because the sample length is increasing during the test, thus, its surface on which the compression is applied increases, which leads to a decrease of the compression stress under constant compression force. There might be also technical limitation in the displacement, which is the case for the present setup (Fig. 1). One way to increase the strain is by cutting the sample into half and shear one part again. Such a test is an interrupted test and can be performed with unlimited repetitions, so extremely large strains can be reached in a small number of steps. An

application of Eq. (11) for such HPCS multipass deformation process is presented in Table 1 for the initial geometry of t_0=2 mm, l_0=10 mm and a shear displacement $_s$=10 mm.

3. Experiments

HPCS experiments were conducted on ARMCO® steel comprised of soft 99.8% iron supplied by Goodfellow Cambridge. The as received samples were in rolled and annealed condition, with an average grain size (surface weighted average) of 38 μm. Two identical samples with dimensions $t_0 = 1.9\,mm$, $l_0 = 9.6$ mm and $w_0 = 20$ mm were positioned on the two sides of the HPCS apparatus plunger. They were sand blasted on their flat surfaces before testing. The corresponding surfaces were also sand blasted on the punch, on the die, and on the plunger. The applied normal loading was set to 35 tons. The resulting normal stress decreased progressively because of the increase of the sample surface area during shearing. The confining force of 8 tons was maintained constant during testing. All punches had a cross section of 20 x 20 mm². The loading forces were continuously recorded together with the displacements of the punches. As the punch displacements were not measured directly at the sample but at the other ends of the punches, the recorded displacements were corrected for the elastic deformations of the punches using Hooke's law with a Young's modulus of 200 GPa. The pushing (driving) punch was moved with a velocity of 0.5 mm/s. The experiments were conducted at room temperature. Multiple-pass experiments were conducted up to three passes, according to the procedure presented in the preceding section; the experimental conditions are given in Table 2. Two first-pass experiments were carried out: test no. 1(a) was done to verify the homogeneity of the deformation process, and the multi-pass testing 1(b)-2(b)-3(b) was made to reach extreme large strains, well into the steady state. In order to verify that no sliding occurred during testing, two fine line-markings were placed perpendicular to the shear direction on the opposite flat surfaces of the samples: they were found to be shifted to each other during shearing exactly with the imposed shearing distance.

After the first and third passes, the samples were sectioned in their mid-width side along the deformation direction (longitudinal cross-section) for both optical microscopy and electron back-scattering diffraction (EBSD) investigations. After sectioning, the samples were mechanically polished with 600, 1200, 1800 and 4000 SiC grit papers. For optical microscopy, the samples

were further polished with 9 μm, 6 μm diamond suspension and final polishing was performed with colloidal silica suspension (Struers' OP-S solution). To reveal microstructure for optical microscopy, these samples were etched with Nital solution (3% HNO_3 and 97% C_2H_5OH). For EBSD, the samples were electrolytically polished with TENUPOL's A2 solution consisting of 700 ml ethanol (C_2H_5OH), 100 ml butyl glycol ($C_6H_{14}O_2$) and 70 ml perchloric acid (60%) (ClO_4). The operating parameters for electrolytic polishing were: 60V, 3.5A for the first pass sample (1.0 mm thickness) and 17V, 1.05A for the third pass sample (0.25 mm thickness) at a flow rate of 20 for 15 seconds at 15-20°C. The EBSD scans were performed by using JEOL JSM-6500F field-emission gun scanning electron microscope. The obtained raw data were processed with the ATEX software [19] to obtain grain sizes, disorientation distributions, crystallographic textures and Inverse Pole Figure (IPF) maps.

4. Experimental results

The initial microstructural state of the as received steel is shown in a longitudinal cross section in Fig. 3. The grain morphology was nearly equiaxed and the texture presented the characteristics of a bcc rolling texture with moderate intensity. During each test the sample thickness decreased significantly, see Table 2, where the accumulated compression, shear and equivalent strains were calculated form Eqs. (4), (7), and (11), respectively. The equivalent stress was obtained from Eq. (24) and the stress-strain response is plotted in Fig. 4. Fig. 1b shows the optical image of the two deformed samples in their longitudinal cross sections after the first pass.

EBSD studies were performed at the central parts of the specimens. For the first pass (test no. 1(a) in Table 2), inverse pole figure maps (IPFs) were measured at three positions across the thickness to reveal possible deformation and microstructure heterogeneities: near to the top and bottom of the sample, as well as in its middle part. Large maps were obtained with dimensions at least 110 μm on each side. Fig. 5a shows the IPF, only for the middle area, for the simple reason that the other two maps (top and bottom areas) were very much similar. Fig. 5b displays the IPF map after the third pass. Grains were detected by imposing a minimum of 5° disorientation across boundaries excluding grains with three pixels and below. For better visualization, the IPF maps were superimposed with the grain boundary networks. For the lower strain, the grain structure was slightly inclined with respect to the shear direction and the grains

were elongated. The inclination angle of the stringers corresponds to the imposed shear value (Fig. 5a). At the higher strain, the stringers are no longer distinguishable (Fig. 5b).

The grain-ellipticity distributions in Fig. 5c cover the whole spectrum for both strain levels. At the lower strain, the maximum probability is at about 0.3 for the top-area and of 0.6 for the middle and bottom areas. At the higher strain it is at about 0.4. Near-equiaxed grains had relatively low occurrence probability for both strains.
The grain sizes were calculated as the equivalent circle diameters of the grains. Their distributions show a single central peak, see Fig. 5d for the area-frequency distribution. The average grain sizes are displayed in Table 3. As can be seen, the grain sizes were submicronic and decreased only slightly from top to bottom across the sample thickness during the first pass. After the third pass, the grain size is only about 200 nm; the difference between the number and surface weighted average sizes is relatively small (Table 3).

The disorientation distributions obtained between neighboring grains are presented in Fig. 5e-f. These distributions were computed between neighboring grains by assigning to a grain its average quaternion orientation in the ATEX Software. It is important to emphasize that they are not pixel-to-pixel disorientations. (The differences between the two kinds of distributions have been discussed in [20].) As can be seen, there are little differences between the disorientation distributions of the three IPF maps after the first pass. They show double peaks, one at about 13° and another at about 47°. The high angle boundary (more than 15°) fractions were 75%, 77%, and 77%, in the top, middle and bottom regions, respectively. After the third pass (Fig. 5f) the disorientation distribution is approaching the random one but significant differences can be observed below 25° and in the range 35°-55°. The relative frequency of the high angle boundaries is more than 92% after the third pass.

The crystallographic textures show the characteristic bcc simple shear texture features (Fig. 6). They are displayed here in form of {110} pole figures as well as in ODF form in two sections of Euler space: in the ϕ_2=0° and 45° sections. While the pole figures display all orientations, the ODF sections contain the main ideal components; listed in Table 4 (for the 45° section). Their positions are also indicated in the pole figures. Note that these textures are statistically well established as they were plotted from large grain number populations obtained by EBSD: more

than 61000 grains from the mid-thickness region of the sample for the first pass, and from about 5000 grains from the third pass.

5. Discussion

In the present study the mechanical analysis of the HPCS has been presented and an application was carried out on an ARMCO® steel. In this section we first discuss the main characteristics of the mechanics in terms of stress, strain, and strain hardening. Then the microstructure will be briefly discussed focusing on the grain fragmentation phenomenon. Finally, the crystallographic texture will be analyzed and the future prospects of HPCS will be presented.

Stress and strain state in HPCS

The main purpose of the present study is to establish the mechanics of the HPCS process. The strain state as well as the stress state have been analysed and each component of the stress and strain tensor defined by analytical expressions. For the calculation of the σ_{11} and σ_{33} normal stress components of the stress tensor, the material behavior was assumed to be von Mises isotropic. This was necessary for obtaining the hydrostatic component of the stress state. Indeed, only the deviatoric stress produces plastic flow of the material, which is the difference between the applied stress and the hydrostatic stress state. The mechanical isotropy hypothesis is acceptable for mild textures, which are actually weak in large strain SPD processes.

The evolution of the hydrostatic and the applied normal stress is displayed in Fig. 7a for the first pass as a function of the equivalent strain together with the strain hardening curve and the evolution of the shear stress component. As can be seen, at the starting point, the normal stress components are equal, so they produce a fully hydrostatic state. As soon as plastic deformation begins, the three normal components evolve differently. The largest component is σ_{22}, which is the applied compressive stress, σ_{33} is smaller, and σ_{11} is the smallest. The difference between the components is produced by the second terms that appear in Eqs. 23a,b. All normal stress components decrease first, then slightly increase from a strain of about 2.4. The decrease in σ_{22} is due to the increase in the surface area of the sample as the compression force was kept constant throughout the HPCS process (35 tons). As can be seen in Eq. 24, the evolution of the

hydrostatic stress is clearly related to the strain evolution of the sample, which is represented by the $\dot{\varepsilon}/\dot{\gamma}$ quantity in Eq. 23. To understand this effect, the evolution of the strain components and the $\dot{\varepsilon}/\dot{\gamma}$ ratio are plotted in Fig. 7b. Both the compression and shear strains increase nearly linearly as a function of the equivalent strain. Inspection of Eqs. 4, 7 and 11 shows that these strain quantities are not actually linear functions of the total equivalent strain. The strain rates also vary as a function of the equivalent strain: the compression strain rate decreases while the shear strain rate increases. These functions are also not strictly linear, only they appear so in Fig. 7b. The evolution of the hydrostatic stress is related to the ratio of the two strain rates, $\dot{\varepsilon}/\dot{\gamma}$, which is also plotted in Fig. 7b. This ratio shows significant evolution during HPCS: it decreases from about -0.2 at the beginning to -0.05 at the end of the test. Now, in order to estimate the relative contributions of the applied compressive force and the shear force to the plastic yielding of the material, we first calculate the deviator tensor starting from its definition:

$$S_{ij} = \sigma_{ij} - \sigma_h \delta_{ij}. \tag{25}$$

With the help of the results obtained in Section 2, we obtain:

$$\underline{\underline{S}} = \begin{pmatrix} -4\tau\dfrac{\dot{\varepsilon}}{\dot{\gamma}} & \tau & 0 \\ \tau & 4\tau\dfrac{\dot{\varepsilon}}{\dot{\gamma}} & 0 \\ 0 & 0 & 0 \end{pmatrix}. \tag{26}$$

This deviatoric stress tensor has two normal and two shear components. The normal stress components originate from the applied compression stress while the shear components arise from the shear forces generated by friction. Their respective contribution to the total flow stress can be represented by their ratio. We define the following ratio for the evaluation of their relative contribution to the total equivalent stress:

$$\rho = \frac{S_{11}}{S_{12}} = -4\frac{\dot{\varepsilon}}{\dot{\gamma}}. \tag{27}$$

Thus, it turns out that the strain rate ratio perfectly defines the ratio of the magnitudes of the two kinds of deviator stresses. The ρ quantity is also plotted in Fig. 7a as a function of the equivalent

strain. It starts at about 0.8 and decreases down to 0.2 by the end of the test during the first pass. Thus, the contribution from the compression force is not far from the shear force at the beginning. Even at the end of testing of the first pass, at the strain of 3.55, the contribution from the compression force remains significant (0.2). The change of stress state is visualized in the S_{11}-S_{12} section of the von Mises yield surface in Fig. 7d where the initial and final stress states are indicated. Note that the effect of strain hardening on the size of the yield surface was omitted in Fig. 7d to better show the relative changes in the stress state. This figure shows also the evolution of the combined stress state for the second and third passes. As can be seen, the stress state approaches the simple shear stress state during the HPCS process. This stress state variation is clearly due to the decrease in the thickness of the sample so that the compression strain becomes nearly negligible with respect to the shear strain during a multiple-pass HPCS testing.

Strain hardening

One of the main advantages of the present HPCS process is the possibility to measure strain hardening during straining. The stress-strain responses displayed in Fig. 4 during the three passes show that the material hardens progressively in each pass. Finally, during the third pass, a steady state regime is attained at a flow stress of 1150 MPa. It is also evidenced by the hardening curves in Fig. 4 that the yield stress is lower at the beginning of subsequent passes. This effect can be attributed to a dislocation recovery process which is activated during the unloading process at the end of the previous pass. Namely, it has been shown experimentally during HPT testing, that there is a large decrease in the vacancy distribution during unloading [21,22] because vacancies are less mobile under high hydrostatic stress, so that they activate dislocation annihilation processes during unloading. Therefore, during subsequent reloading, there is less number of dislocations in the material which leads to a lowering of the flow stress. Hosakawa et al. [23] estimate linear work hardening during HPT in pure iron up to a shear strain of 57 (von Mises equivalent strain of 32.9) and found a flow stress level of 1130 MPa during HPT which is nearly the same as in our experiments. (Note that Hosokawa et al. presented their results using the Hencky strain measure which is shown to be invalid for simple shear in [23,24] . Nevertheless, the Hencky strain can be converted back into shear strain using the formula presented in the Appendix, so comparisons are possible.)

Once the steady state regime is reached in strain hardening, the average grain size remains constant. It has been shown by Pougis et al. [25] that the steady state in SPD processes

corresponds with an extension of the so-called Derby-plot [26, 27] constructed for dynamic recrystallization. In the Derby-plot the flow stress is normalized by the shear modules and plotted as a function of the average grain size normalized by the Burgers vector, in a double logarithmic presentation. For the steady state in the case of the present ARMCO® steel we obtain the following Derby coordinates: $\bar{\sigma} / \mu = 0.0126$ and $\bar{d} / b = 809$. This point lies exactly on the Derby-line (see the Derby figure extended for the UFG domain in Ref. [25]). The occurrence of dynamic recrystallization is evidence of the steady state, not only from the agreement with the Derby-plot but also by examining the microstructure in the steady state, see the IPF map in Fig. 5b. The very small grain size and the large deviation from the expected very elongated grain shape provide clear evidence of grain subdivision and grain boundary migration. The existence of a small peak on the hardening curve in Fig. 4 at the beginning of the third pass is also an indication of the occurrence of dynamic recrystallization; typical in strain hardening curves when DRX becomes the major mechanism of the microstructure evolution.

It is well established that strain hardening can be analyzed by plotting the rate of hardening as a function of the stress, called also the Kocks-Mecking plot, as shown in Fig. 7c. (The derivatives of the hardening curves were obtained by first fitting the hardening curves by a polynomial function.) Fig. 7c shows clearly Stages III and IV during which the strain hardening rate decreases. During the third pass, it even reaches the zero value, i.e. the steady state. In each pass both stages III and IV appear, each time shifted parallel to a higher stress level. This is the consquence of the unloading and reloading sequences between passes. As discussed above, a dislocation annihilation process takes place when the large hydrostatic stress is removed from the sample. A consequence of this dislocation density reduction is that the microstructure is no longer in its equilibrium state for remaining in the preceding Stage IV state, so that to reach again Stage IV, first the dislocation density has to be recovered by further strain hardening, necessarily in Stage III. Stage IV is reached in each pass; the longest one in the third pass. Finally, Stage IV ends and the steady state stage is reached. This last stage is called Stage VI in Ref. [28] because to arrive at a constant stress level there has to be a transition stage between the linear and no hardening stages; which is called Stage V in Ref. [28].

Grain refinement and microstructure

The main characteristics of the microstructures obtained by SPD processes is their extreme refinement. In this study, the average grain size of the steel was refined by the HPCS-induced

equivalent strain of 33 from the as received number average size of 31.1 μm to 180 nm, a reduction by approximately 170 times. By comparison Pippan et al. [29] report 150 nm grain size at the same equivalent strain in ARMCO® steel. Hosokawa et al. [23] report at about the same strain value a grain size of 300 nm after High Pressure Torsion to 0.85 mm thick electrolytic pure Fe discs with 12 ppm carbon.

Our study after the first pass shows that the degree of refinement was essentially uniform through the thickness, see Table 3. Furthermore, the angle of the elongated grain structure with respect to the shear direction was also identical in the top, middle, and bottom regions observed (only the middle region is shown in Fig. 5a as the others are very similar). Additional evidence of the uniformity of shear through the thickness of the strip can be found in disorientation distributions shown for top, middle, and bottom regions in Figure 5e.

Crystallographic texture

The crystallographic textures measured after one pass at three places in the cross section of the deformed sample appear to be characteristic bcc shear textures (only the mid-section is shown to save space in Fig. 6). It is also the case after the third pass. All ideal components appear, with different intensities with respect to each other. The texture intensity is relatively low which means that anisotropy is relatively small, supporting the use of the von Mises isotropic yield surface in the mechanical analysis. It is an interesting fact that the compression strain component during HPCS has no detectable effect on the texture evolution; the textures are really like ideal simple shear textures. This might be due to the relatively small value of the accumulated equivalent strain in compression (-0.6 during the first pass and -0.94 after the third) with respect to the equivalent strain corresponding to the simple shear component of the deformation (3.55 and 21.1, respectively). The deformation path also supports the tendency towards a fully simple shear deformation mode, which was evidenced by the movement of the loading point on the von Mises yield surface in Fig. 7d.

Perspectives

HPCS is shown to be an efficient way to deform metals to large strains. While the stress and strain rate state is multiaxial, it is readily possible to obtain equivalent stress-strain curves. As can be seen in Table 1, during multipass HPCS process the strain accummulates extremely

rapidly, after only two passes, the strain is already 13.1. As a comparison, 16 passes would be needed to reach the same strain in the ARB process, or 11 in 90° ECAP.

It is also possible to change the strain path between passes by rotating the sample around either the shear direction or the plane normal. Thus, similar to ECAP, different routes can be established.

6. Conclusions

A new variant of the HPS process was established in the present paper, called HPCS. First the mechanics of the process were examined. All stress and strain components were expressed in analytical form (except the applied compression and applied shear forces, measured directly). HPCS was applied to ARMCO® steel in an apparatus in which the shear force, normal force, and shearing distance could be monitored to allow the stress-strain response to be measured *in situ* into the steady state work hardening regime. The crystallographic texture and the microstructure was examined by EBSD. The results presented substantiate the following main conclusions:

1. The HPCS deformation process was established experimentally in a setup different from the originally proposed HPS process [8] using a three axis extrusion machine. The new feature is a significant decrease in the thickness of the sample during large strain shearing. Both the stress and strain states are multiaxial in the proposed HPCS setup.
2. The applied compression stress does not result in a purely hydrostatic stress state in HPCS: an analytical formula was developed for the deviator stress tensor assuming von Mises isotropic flow. The deviatoric stress state progressively approaches the simple shear stress state as a function of strain.
3. Multi-pass experiments were carried out on ARMCO® steel, well into the steady state of strain hardening at 1150 MPa which defines a point on the Derby-plot of dynamic recrystallization. The microstructure features also suggested that dynamic recrystallization took place in the steady state, at room temperature.
4. A characteristic bcc simple shear texture was obtained via HPCS of ARMCO® steel.
5. The grain size was reduced by about a factor of 170 upon reaching steady state flow conditions. The grain size distributions, grain ellipticity, crystallographic texture, and

crystallographic disorientation distributions were uniform throughout the thickness of the samples.

7. Acknowledgements

The authors acknowledge the help received from Prof. Yan Beygelzimmer (Donetsk Institute for Physics and Engineering, Ukraine) for the integration of Eq. (10) that led to Eq. (11). This work was supported by the French State through the program "Investment in the future" operated by the National Research Agency (ANR) and referenced by ANR-11-LABX-0008-01 (LabEx DAMAS). Viet Q. Vu acknowledges the PhD scholarship awarded by the Vietnamese Government (Project 911).

Appendix

Conversion of the Hencky strain into shear strain

During large strain simple shear, the grain shape changes from an initially spherical one into a very elongated ellipse. This shape change motivated the establishment of the so-called Hencky strain (h_{eq}) which is the von Mises equivalent strain calculated from the two logarithmic principal strains of the two axes of the ellipse resulting from their length changes [31]:

$$h_{eq} = \frac{1}{\sqrt{3}} \ln\left(\frac{2+\gamma^2+\gamma\sqrt{4+\gamma^2}}{2} \right) \quad . \tag{A1}$$

This strain measure, however, has been proven to be inappropriate to characterize the strain state during simple shear because it neglects the rotation of the ellipse [32] , and does not satisfy the principles imposed by the group theory [28] . Nevertheless, because of the large number of papers that used the Hencky strain, it is useful to make the conversion between the Hencky strain and the correct equivalent strain.

From the above Hencky strain equation one can readily express the γquantity:

$$\gamma = \frac{e^{h_{eq}\sqrt{3}} - 1}{\sqrt{e^{h_{eq}\sqrt{3}}}} \ . \tag{A2}$$

Using this formula, one can convert the Hencky strain into shear strain, so all published results that used the Hencky strain can be used in other works. Further, the shear value can be converted into the von-Mises equivalent strain:

$$\bar{\varepsilon}_{vM} = \gamma\sqrt{3} \ . \tag{A3}$$

The difference between the two strain measures is very high for large strains. For example, in HPT testing, after one turn of a disk of 1 mm thickness and 20 mm in diameter, the simple shear formula gives at the outer radius a shear of 125.7, which is in Hencky strain $h_{eq} = 5.58$, while from Eq. (A2) we obtain: $\bar{\varepsilon}_{vM} = 72.6$.

Data availability statement:

The experimental data will be provided upon request.

References

[1] Y. Estrin, A. Vinogradov, Extreme grain refinement by severe plastic deformation: A wealth of challenging science, Acta Mater. 61 (2013) 782-817.

[2] V.M. Segal, Materials processing by simple shear, Mater. Sci. Eng. A 197 (1995) 157-164.

[3] A.P. Zhilyaev, T.G. Langdon, Using high-pressure torsion for metal processing: Fundamentals and applications, Prog. Mater. Sci. 53 (2008) 893-979.

[4] Y. Saito, H. Utsunomiya, N. Tsuji, T. Sakai, Novel ultra-high straining process for bulk materials-development of the accumulative roll-bonding (ARB) process, Acta Mater. 47 (1999) 579-583.

[5] S. Panda, L.S. Toth, J.-J. Fundenberger, O. Perroud, J. Guyon, J. Zou, T. Grosdidier, Analysis of heterogeneities in strain and microstructure in aluminum alloy and magnesium processed by high-pressure torsion, Mater. Charact. 123 (2017) 159-165.

[6] L.S. Tóth, M. Arzaghi, J.J. Fundenberger, B. Beausir, O. Bouaziz, R. Arruffat-Massion, Severe plastic deformation of metals by high-pressure tube twisting, Scr. Mater. 60 (2009) 175-177.

[7] A. Pougis, L.S. Tóth, O. Bouaziz, J.J. Fundenberger, D. Barbier, R. Arruffat, Stress and strain gradients in high-pressure tube twisting, Scr. Mater. 66 (2012) 773-776.

[8] T. Fujioka, Z. Horita, Development of high-pressure sliding process for microstructural refinement of rectangular metallic sheets, Mater. Trans. 50 (2009) 930-933.
[9] S. Lee, K. Tazoe, I.F. Mohamed, Z. Horita, Strengthening of AA7075 alloy by processing with high-pressure sliding (HPS) and subsequent aging, Mater. Sci. Eng. A 628 (2015) 56-61.
[10] T. Masuda, Y. Takizawa, M. Yumoto, Y. Otagiri, Z. Horita, Extra strengthening and superplasticity of ultrafine-grained A2024 alloy produced by high-pressure sliding, J. Jpn. I. Met. Mater. 80 (2016) 593-601.
[11] Y. Takizawa, K. Sumikawa, K. Watanabe, T. Masuda, M. Yumoto, Y. Kanai, Y. Otagiri, Z. Horita, Incremental feeding high-pressure sliding for grain refinement of large-scale sheets: application to Inconel 718, Metall. Mater. Trans. A 49 (2018) 1830–1840.
[12] Y. Takizawa, T. Kajita, P. Kral, T. Masuda, K. Watanabe, M. Yumoto, Y. Otagiri, V. Sklenicka, Z. Horita, Superplasticity of Inconel 718 after processing by high-pressure sliding (HPS), Mater. Sci. Eng. A 682 (2017) 603-612.
[13] K. Tazoea, S. Hondab, Z. Horita, Application of high-pressure sliding for grain refinement of Al and Mg alloys, Mater. Sci. Forum 667-669 (2011).
[14] Z. Horita, Severe plastic deformation under high pressure for production of superplastic materials, Mater. Sci. Forum 838-839 (2016) 287-293.
[15] T. Masuda, K. Fujimitsu, Y. Takizawa, Z. Horita, High-pressure sliding using rod samples for grain refinement and superplasticity in Al and Mg alloys, Lett. on Mater. 5 (2015) 258-263
[16] Y. Takizawa, T. Masuda, K. Fujimitsu, T. Kajita, K. Watanabe, M. Yumoto, Y. Otagiri, Z. Horita, Scaling up of high-pressure sliding (HPS) for grain refinement and superplasticity, Metall. Mater. Trans. A 47 (2016) 4669–4681.
[17] N.Q. Chinh, G. Horváth, Z. Horita, T.G. Langdon, A new constitutive relationship for the homogeneous deformation of metals over a wide range of strain, Acta Mater. 52 (2004) 3555-3563.
[18] F. Wetscher, A. Vorhauer, R. Pippan, Strain hardening during high pressure torsion deformation, Mater. Sci. Eng. A 410-411 (2005) 213-216.
[19] B. Beausir, J.-J. Fundenberger, Analysis tools for electron and X-ray diffraction, ATEX - software, www.atex-software.eu, Université de Lorraine - Metz, 2017.
[20] L.S. Toth, C. Gu, Ultrafine-grain metals by severe plastic deformation, Mater. Charact. 92 (2014) 1-14.
[21] E. Schafler, Scripta Mater. 64 (2011) 130.
[22] E. Schafler, Scripta Mater. 62 (2010) 423.
[23] A. Hosokawa, H. Ohtsuka, T. Li, S. Ii, and K. Tsuchiya, Microstructure and Magnetic Properties in Nanostructured Fe and Fe-Based Intermetallics Produced by High-Pressure Torsion, Mater. Trans., vol. 55, no. 8, pp. 1286–1291, Aug. 2014.
[24] A. Hosokawa, S. Ii, K. Tsuchiya, Work hardening and microstructural development during high-pressure torsion in pure Iron, Mater. Trans. 55 (2014) 1097-1103.
[25] A. Pougis, L.S. Toth, J.J. Fundenberger, A. Borbely, Extension of the Derby-relation to metals severely deformed to their steady state ultra-fine grain size, Scripta Mater. 72-73 (2014) 59-62.
[26] B. Derby, Acta Metall. Mater. 39 (1991) 955.
[27] B. Derby, Scripta Metall. Mater. 27 (1992) 1581.
[28] Y. Beygelzimer, L.S. Toth, J.J. Jonas, Some physical characteristics of strain hardening in severe plastic deformation, Adv. Eng. Mater. 17 (2015) 1783-1791.

[29] Reinhard Pippan, Florian Wetscher, Martin Hafok, Andreas Vorhauer, and Ishaf Sabirov, The Limits of Refinement by Severe Plastic Deformation, Advanced Engineering Materials 8 (2006), DOI: 10.1002/adem.200600133.
[30] J. Baczynski, J.J. Jonas, Texture development during the torsion testing of α-iron and two IF steels, Acta Mater. 44 (1996) 4273-4288.
[31] S. Onaka, Equivalent strain in simple shear deformation described by using the Hencky strain, Philos. Mag. Lett. 90 (2010) 633-639.
[32] J.J. Jonas, C. Ghosh, V. Basabe, S. Shrivastava, The Hencky equivalent strain and its inapplicability to the interpretation of torsion testing experiments, Philos. Mag. 92 (2012) 2313-2328.

(a)

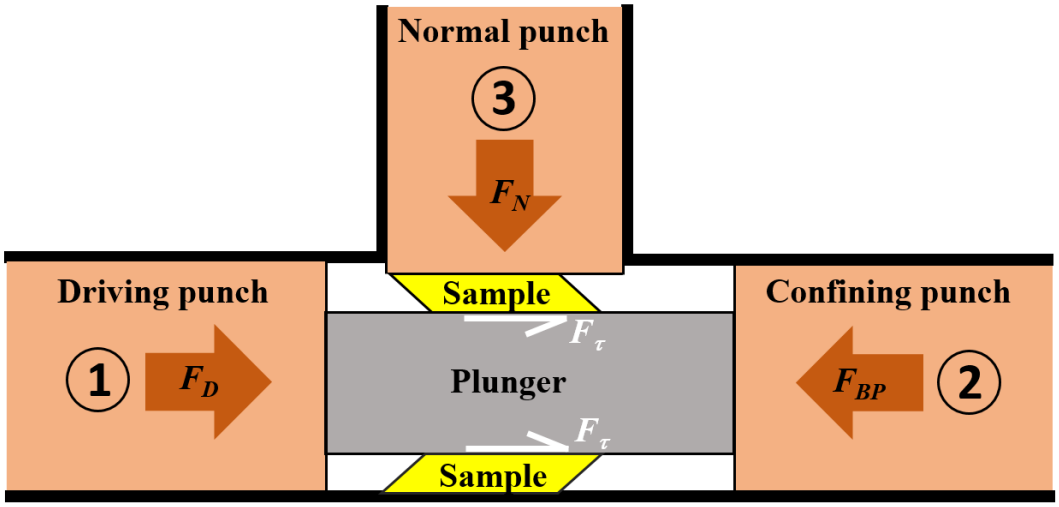

(b)

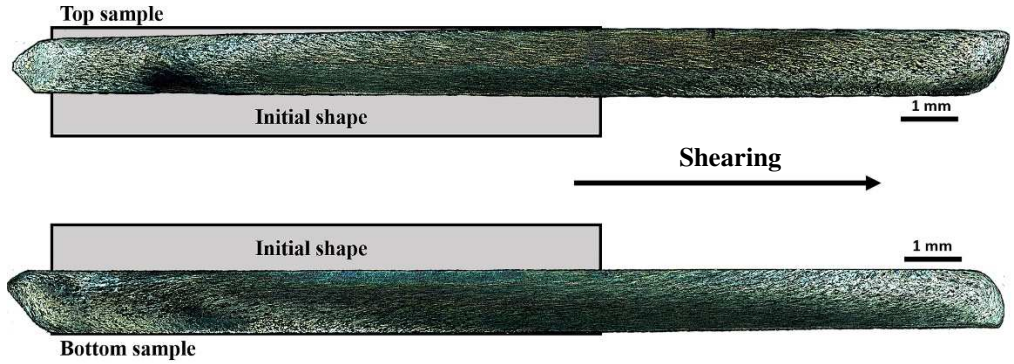

Fig. 1. (a): Schematic figure for the experimental HPCS setup. (b): The two samples after the first pass deformation.

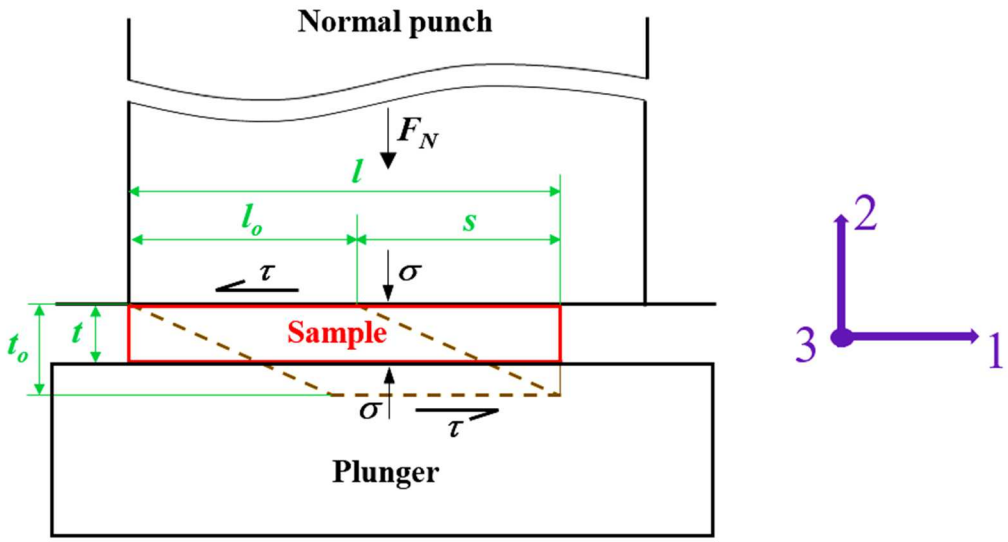

Fig. 2. Schematic figure showing the dimensions and the forces applied on the upper specimen

(a)

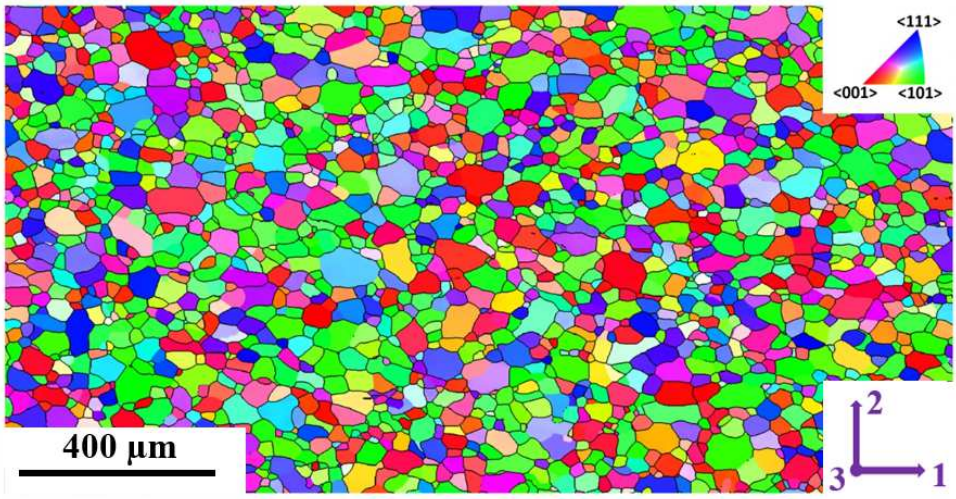

(b)

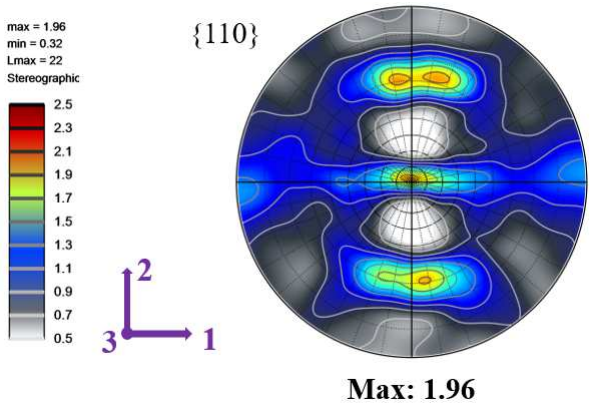

Fig. 3. The initial grain-state of the material (a) and its crystallographic texture in a {110} pole figure (b).

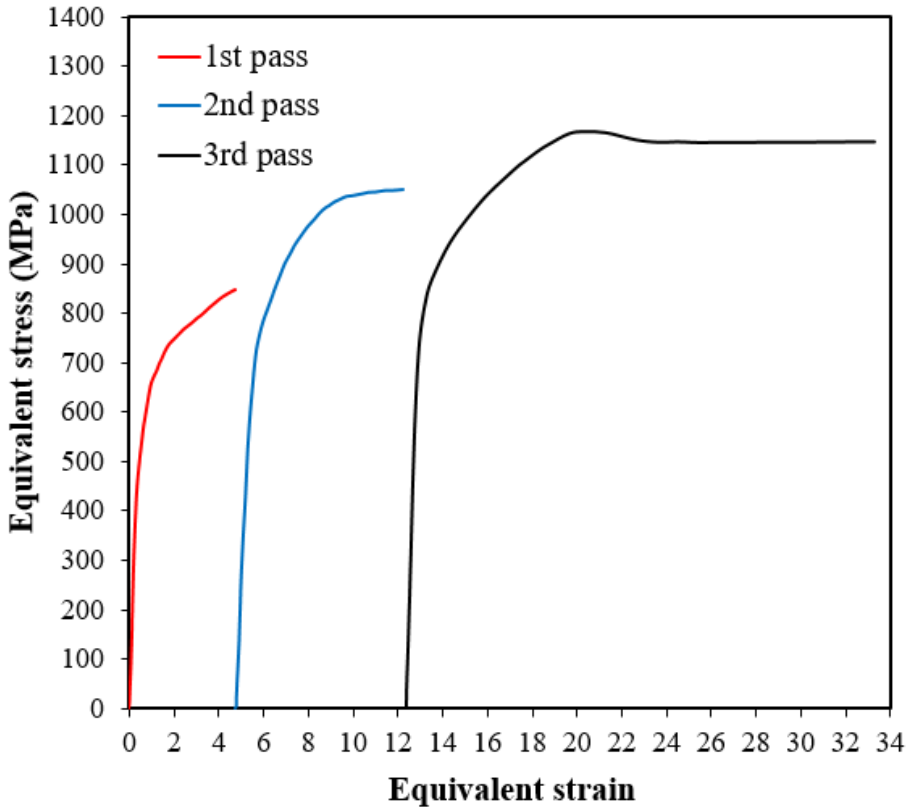

Fig. 4. Stress–strain curves obtained by HPCS for ARMCO® steel in three consecutive passes up to an equivalent strain of 33.34.

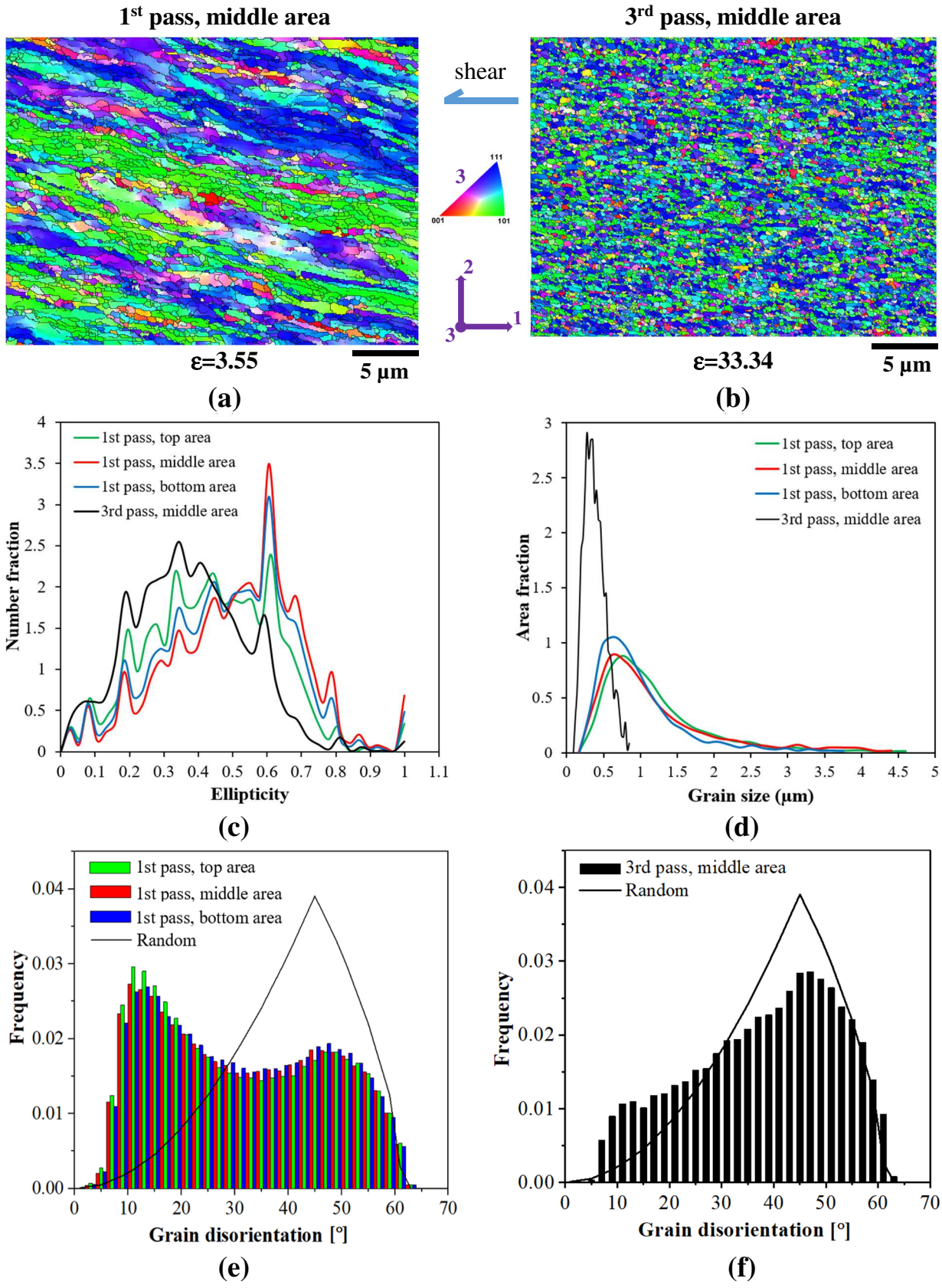

Fig. 5. (a)-(b): IPF maps after the first and third passes. (c)-(d): Ellipticity and grain size distributions. (e)-(f): Next-neighbor disorientation distributions.

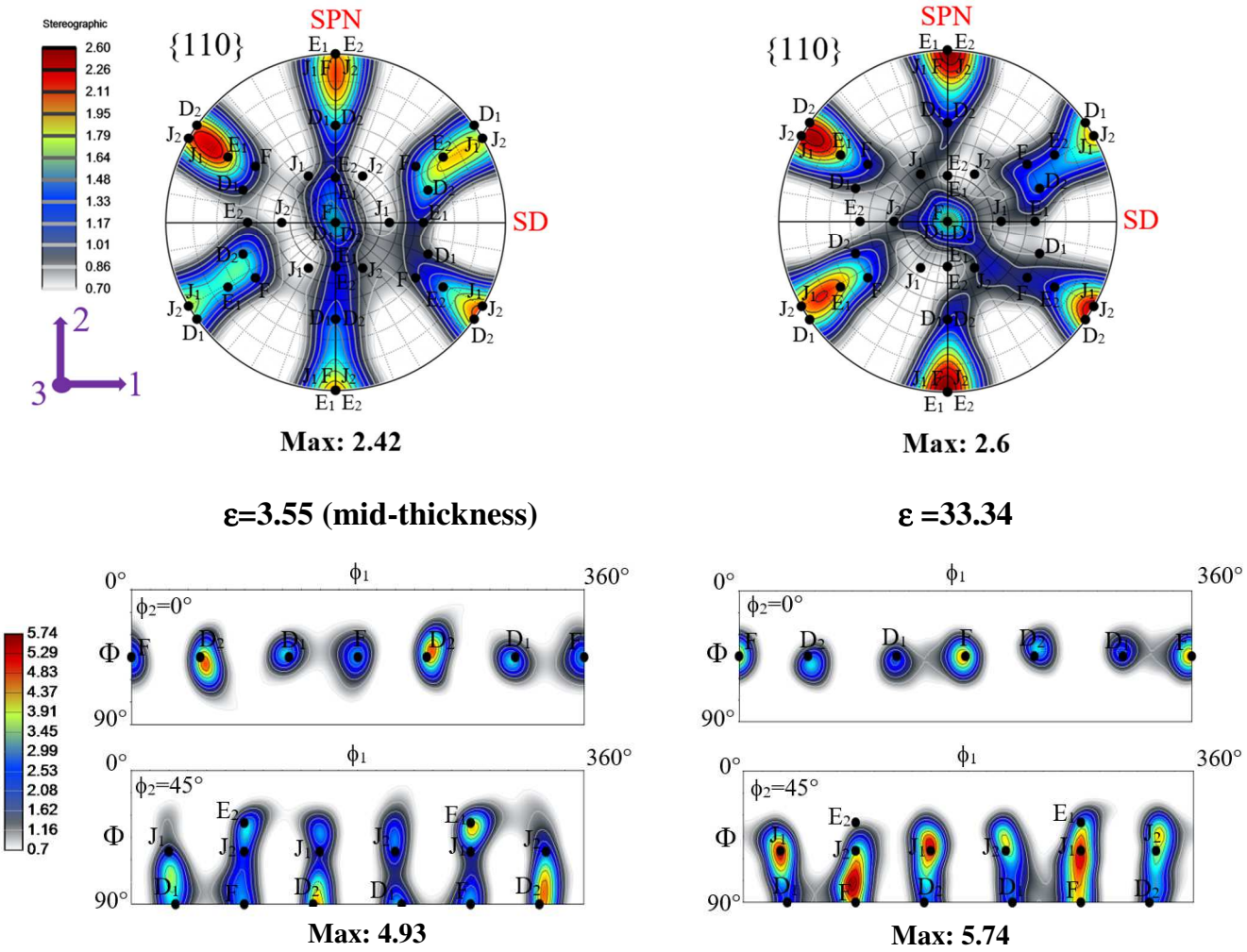

Fig. 6. The crystallographic textures in {110} pole figures, and the ODFs in two sections of the Euler orientation space (top row: ϕ_2=0°, bottom row: ϕ_2=45°). SPN and SD denote the orientations of the shear plane normal and the shear direction, respectively.

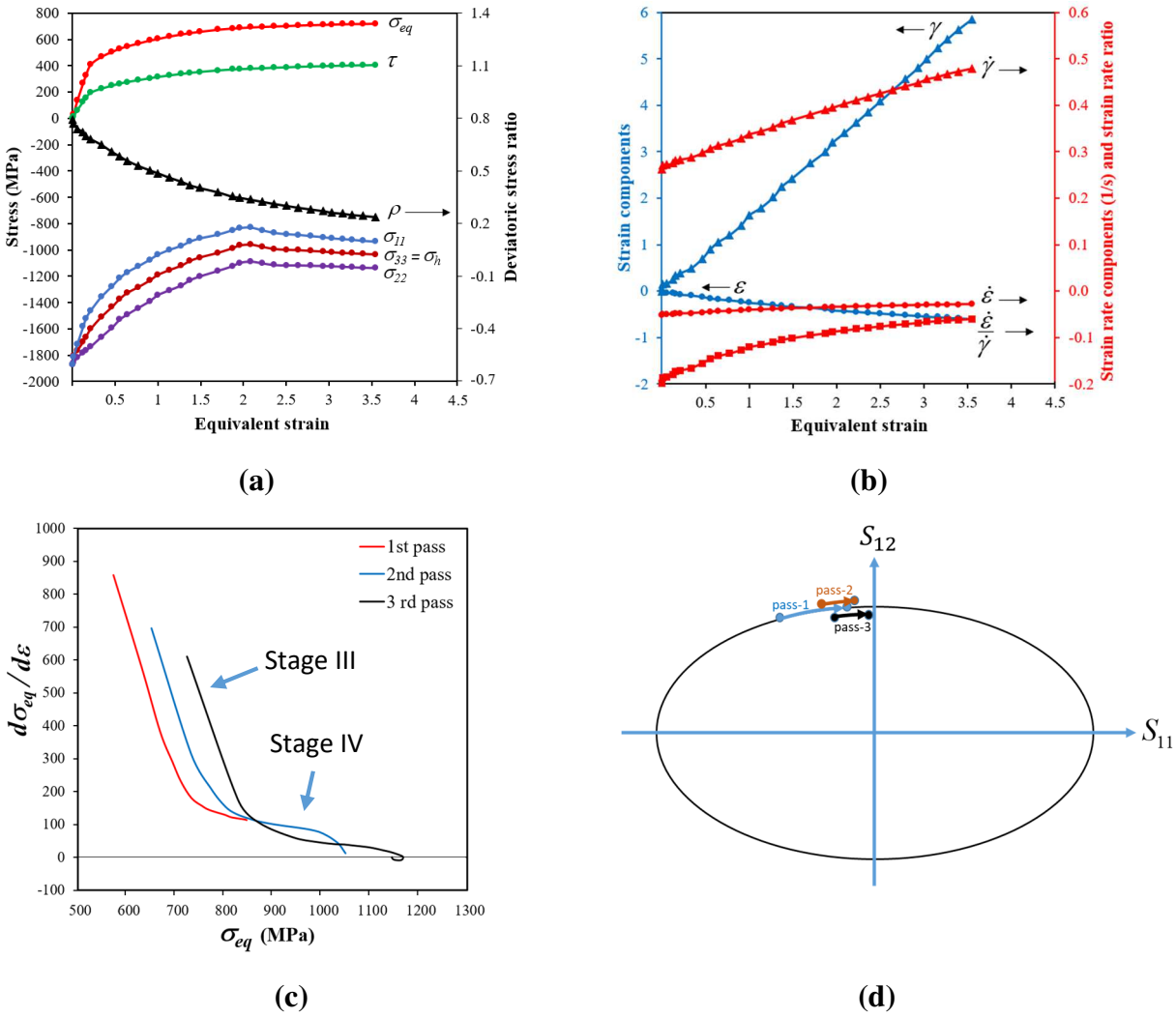

Fig. 7. (a): The evolution of the non-zero stress components of the stress tensor during HPCS of ARMCO® steel during the first pass. The value of the hydrostatic stress σ_h is equal to σ_{33}. The curve indicated by τ is the shear stress. ρ is the ratio of the deviator stresses corresponding to the compression and the shear. (b): The shear and compression strains as a function of the equivalent strain during the first pass. (c): The rate of strain hardening as a function of stress ('Kocks-Mecking plot') from (a). (d): The evolution of the stress state during HPCS of ARMCO® steel in the S_{11}-S_{12} section of the von Mises yield surface.

Table 1. The equivalent strain and the sample thickness in multipass HPCS for the initial geometry t_0=2 mm, l_0=10 mm and a shear displacement s=10 mm.

Pass number	Equivalent strain	Sample thickness at the end of the pass [mm]
1	4.4	1.0
2	13.1	0.5
3	30.4	0.25
4	64.9	0.125
5	133.9	0.0625

Table 2. The parameters of the multi-pass HPCS testing on ARMCO® steel.

	Initial thickness (mm)	Initial length (mm)	Displacement (mm)	Thickness at end of pass (mm)	Normal force (ton)	Confining force (ton)	Compression strain in one pass	Shear strain in one pass	Equivalent strain in one pass	Accum. equiv. strain
1(a)	1.9	9.6	8	1.04	35	8.5	-0.6	5.8	3.55	3.55
1(b)	1.9	9.7	9.5	0.96	40	8.5	-0.68	7.6	4.74	4.74
2(b)	0.96	9.5	8.4	0.51	45	8.5	-0.63	12	7.2	11.94
3(b)	0.51	5.8	9	0.2	50	8.5	-0.94	39.5	21.12	33.34

Table 3. Average grain sizes obtained after HPCS of ARMCO® steel. Unit is [nm].

	Pass 1(a), top region	Pass 1(a), middle part	Pass 1(a), bottom region	Pass 3
Number-weighted [nm]	555	476	464	181
Surface-weighted [nm]	664	586	550	218

Table 4. The Miller indices of the main ideal orientations of simple shear textures for BCC materials and their location in the ϕ_2=45° section of Euler orientation space (for shear in direction of axis 1 and with shear plane normal oriented in direction 2) [30].

	D_1	D_2	E_1	E_2	F	J_1	J_2
	$(11\bar{2})[111]$	$(\bar{1}\bar{1}2)[111]$	$(01\bar{1})[111]$	$(0\bar{1}1)[111]$	$(110)[001]$	$(0\bar{1}1)[\bar{2}11]$	$(1\bar{1}0)[\bar{1}\bar{1}2]$
ϕ_1 (°)	125.3	54.7	39.2	90	180	30	90
ϕ (°)	45	45	65.9	35.3	45	54.7	54.7
ϕ_2 (°)	45	45	45	45	45	45	45

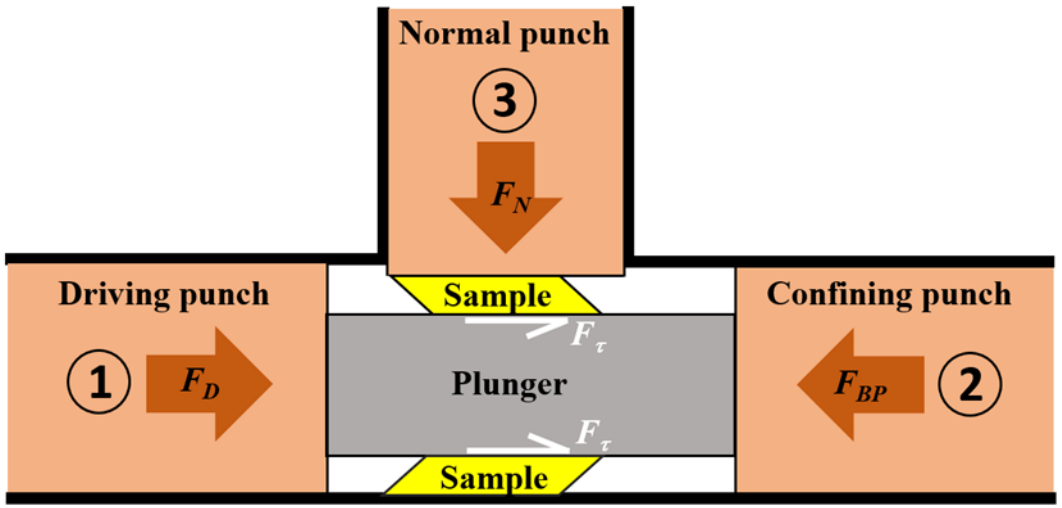
Normal punch
3
F_N
Sample
Driving punch
1
F_D
F_τ
Plunger
F_τ
Confining punch
F_{BP}
2
Sample

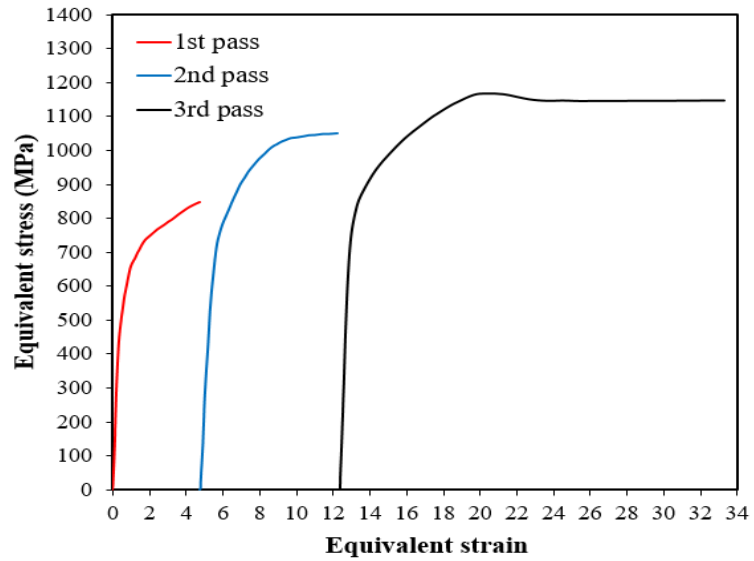
1st pass
2nd pass
3rd pass
Equivalent stress (MPa)
Equivalent strain
0
100
200
300
400
500
600
700
800
900
1000
1100
1200
1300
1400
0 2 4 6 8 10 12 14 16 18 20 22 24 26 28 30 32 34